

## FINITE ELEMENT MODELING OF WELDED JOINTS

**Andrés Anca, Alberto Cardona and Víctor Fachinotti**

*Centro Internacional de Métodos Computacionales en Ingeniería (CIMEC-INTEC), Universidad Nacional del Litoral - CONICET, Güemes 3450, CP 3000 Santa Fe, Argentina, [aanca@intec.unl.edu.ar](mailto:aanca@intec.unl.edu.ar), <http://www.cimec.org.ar>*

**Keywords:** Finite Elements, Welding Simulation, Computational Mechanics.

**Abstract.** This work deals with the simulation of fusion welding by the Finite Element Method. The implemented models include moving heat sources, temperature dependence of thermo-physical properties, elasto-plasticity, non-steady state heat transfer, and mechanical analysis. It is assumed that the thermal problem is not coupled with the mechanical one, being the thermal analysis performed separately and prior to the mechanical analysis. The mechanical problem is based on thermal history. A special treatment is performed on mechanical elements during the liquid/solid and solid/liquid phase changes. The three-dimensional stress state of a butt-welded joint is obtained as an example of application..

## 1 INTRODUCTION

The use of the Finite Element Method (FEM) in product development is now well established, however, its use in manufacturing processes is not very common and is part of the field of new applications in computational mechanics. The most important reason for this development is the industrial need to improve productivity and quality of products and to have better understanding of the influence of different process parameters. The modeled phenomena play an important role at various stages of the production of steel parts, for example, welding, heat treatment and casting, among others.

The importance of these applications lies in determining the evolution of stresses and deformations to predict, for example, susceptibility to cracking and thus prevent failures during manufacturing or even service. Furthermore, this simulation tool can be used to optimize some aspects of manufacturing processes.

Welding is defined by the American Welding Society (AWS) as a localized coalescence of metals or non-metals produced by either heating of the materials to a suitable temperature with or without the application of pressure, or by the application of pressure alone, with or without the use of filler metal (Mackerle, 2004). Welding techniques are one of the most important and most often used methods for joining pieces in industry. Any information about the shape, size and residual stress of a welded piece is of particular interest to improve quality.

The analysis of welding processes involves several branches of Physics, and requires the coupling of different models addressed to describe the behavior of a phenomenological system. Many of these models have been implemented numerically and are being used in an efficient way to solve the problems on an individual basis.

In the arc welding process, the energy required for metal fusion is produced by Joule effect. This effect produces the energy required to melt the base and filler metal, forming what is known as the liquid pool. The piece surface temperature varies from 1700 K to 2500 K, depending on the material. In the liquid pool, convective effects take place, what improve the heat transport in the base metal. Finally, after removing the heat sources, the metal solidifies.

During the process, temperature changes in the alloy produce solid state transformations. These microstructural transformations cause changes in the material properties during the evolution of the process. Heating and cooling induce localized volumetric changes. The thermal strains that occur in the vicinity of the welding zone are elastoplastic and the resulting stresses react causing permanent distortions.

Distortions introduce residual deformation that complicates the assembly of welded structures and reduces their quality. Also, in certain applications, this distortion may bring the structure useless .

The article is organized as follows. First in Section 2 we describe briefly the coupled thermo-mechanical problem. In Section 3 and 4 we describe the developed model for the thermal and mechanical problems, their hypotheses and the equations involved and also the discretization procedure to obtain the set of equations in both fields. Finally in Section 6 the stress distribution in a butt-welded joint is modeled as an application example.

## 2 COUPLINGS BETWEEN FIELDS

In this section, couplings concerned with the thermal and mechanical effects are summarized. The couplings to be considered are:

1. Material properties depending on the temperature field.

## 2. Thermal expansion and temperature dependent material properties.

The heat generated by the plastic deformation is much less than the heat introduced by the weld arc. Therefore, the thermal analysis may be performed separately from the mechanical analysis.

This approach included the latent heats for the liquid/solid phase transformations and temperature dependencies of the heat capacity and conductivity, but the solid state transformations effects are not included. Finally, the adopted coupling scheme is summarized in Figure 1.

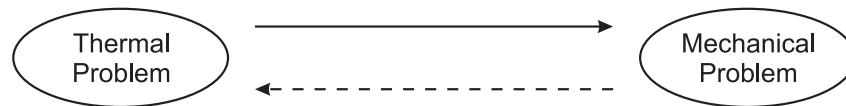


Figure 1: Thermo-mechanical coupling.

## 3 THERMAL PROBLEM

In this section a temperature-based finite element model to simulate unsteady conduction heat transfer problems in a 3D media undergoing mushy phase change is described.

The analyzed domain is discretized using linear tetrahedral finite elements. Galerkin weighting functions are used.

During phase change, a considerable amount of latent heat is released or absorbed, causing a strong non-linearity in the enthalpy function. In order to model correctly such phenomenon, we distinguish the different one-phase subregions encountered when integrating over those finite elements embedded into the solidification front.

Contributions from different phases are integrated separately in order to capture the sharp variations of the material properties between phases. This, so called, discontinuous integration avoids the regularization of the phenomenon, allowing the exact evaluation of the discrete non-linear governing equation, which is solved using a full Newton-Raphson scheme, together with line-search.

We validated the performance of the thermal model by comparison with the exact solution of [Özsisik and Uzzell \(1979\)](#).

### 3.1 Problem definition

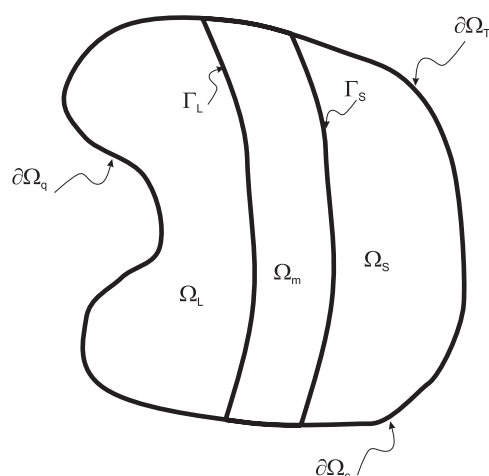


Figure 2: Thermal problem definition.

Under the assumptions of incompressibility, negligible viscosity and dissipation, linear dependence of the heat flux on temperature gradient (Fourier's law), and no melt flow during the solidification process, the energy balance for each subdomain  $\Omega_i$  is governed by the classical energy balance equation

$$\rho \frac{\partial \mathcal{H}}{\partial t} - \nabla \cdot (\kappa \nabla T) = q \quad \forall (\mathbf{x}, t) \in \Omega_i \quad (1)$$

where  $T$  denotes the temperature,  $\mathcal{H}$  the enthalpy (per unit volume),  $\kappa = \kappa(T)$  the material thermal conductivity, assumed isotropic and  $q = q(\mathbf{x}, t)$  is the welding volume heat input (to be defined later in Section (3.4) in the context of welding analysis). Equation (1) is supplemented by the following initial condition

$$T = T_0 \quad \forall \mathbf{x} \in \Omega_i, \quad t = t_0$$

and the external boundary conditions on  $\partial\Omega$ :

$$T = \bar{T} \quad \text{at } \partial\Omega_T \quad (2)$$

$$-\kappa \nabla T \cdot \mathbf{n} = \bar{q} \quad \text{at } \partial\Omega_q \quad (3)$$

$$-\kappa \nabla T \cdot \mathbf{n} = h_{env}(T - T_{env}) \quad \text{at } \partial\Omega_c \quad (4)$$

being  $\partial\Omega_T$ ,  $\partial\Omega_q$  and  $\partial\Omega_c$  non-overlapping portions of the body boundary  $\partial\Omega$ , with prescribed temperature, conductive and convective heat flux, respectively. In the above,  $\bar{T}$  and  $\bar{q}$  refer to imposed temperature and heat flux fields, and  $T_{env}$  is the temperature of the environment, whose film coefficient is  $h_{env}$ ;  $\mathbf{n}$  denotes the unit outward normal to  $\partial\Omega$ .

Further, the following continuity conditions must hold at the interface(s)  $\Gamma$ :

$$T = T_\Gamma \quad (5)$$

$$\langle \mathcal{H}u(\boldsymbol{\eta}) + \kappa \nabla T \cdot \boldsymbol{\eta} \rangle = 0 \quad (6)$$

where  $T_I$  is a constant value (equal to the melting temperature for isothermal solidification, and either the solidus or liquidus temperature otherwise),  $\langle * \rangle$  denotes the jump of the quantity  $(*)$  in crossing the interface  $\Gamma$ , which is moving with speed  $u$  in the direction given by the unit vector  $\boldsymbol{\eta}$ . Note that the second equation states the jump energy balance at the interface.

In order to retrieve  $T$  as the only primal variable, enthalpy is defined as

$$\mathcal{H}(T) = \int_{T_{ref}}^T \rho c d\tau + \rho \mathcal{L} f_l \quad (7)$$

being  $\rho c$  and  $\rho \mathcal{L}$  the unit volume heat capacity and latent heat, respectively, and  $T_{ref}$  an arbitrary reference temperature;  $f_l$  is a characteristic function of temperature, called volumetric liquid fraction, defined as

$$f_l(T) = \begin{cases} 0 & \text{if } T < T_{sol} \\ 0 \leq f_l^m(T) \leq 1 & \text{if } T_{sol} \leq T \leq T_{liq} \\ 1 & \text{if } T > T_{liq} \end{cases} \quad (8)$$

where  $T_{sol}$  and  $T_{liq}$  denote the solidus and liquidus temperatures, respectively, i.e., the lower and upper bounds of the mushy temperature range.

### 3.2 Finite element formulation

First, the weak or variational form of the balance equation (1) is derived, supplied by the boundary conditions (2-6), using the weighted residuals method. The proper choice of weighting functions together with the application of Reynolds' transport theorem allows to cancel the terms arising from the interface conditions (6). Furthermore, using the definition (7), a weak temperature-based form of the governing equation is obtained:

$$\begin{aligned} \int_{\Omega} W \rho c \frac{\partial T}{\partial t} dV + \frac{\partial}{\partial t} \int_{\Omega} W \rho \mathcal{L} f_l dV + \int_{\Omega} \kappa \nabla W \cdot \nabla T dV + \int_{\partial \Omega_q} W \bar{q} dS + \\ + \int_{\partial \Omega_c} W h_{env} (T - T_{env}) dS - \int_{\Omega} W q dV = 0 \end{aligned} \quad (9)$$

where  $W$  is the weighting function.

In the finite element context, the unknown field  $T$  is approximated as a linear combination of interpolation functions  $N_i(x, y, z)$ , the shape functions, as follows:

$$T(x, y, z) = \sum_i^N N_i(x, y, z) T_i \quad (10)$$

being  $T_i$  the temperature at each node  $i$  ( $i = 1, 2, \dots, N$ ) arising from the discretization of the analyzed domain  $\Omega$ .

We substitute  $T$  by its approximation (10) into equation (9). Then we adopt as weighting function  $W$  the interpolation function  $N$  ( $W \equiv N_i$ , Galerkin method). A non linear system of  $N$  ordinary differential equations is set, stated in matrix form as

$$\boldsymbol{\Psi} = \mathbf{C} \frac{\partial \mathbf{T}}{\partial t} + \frac{\partial \mathbf{L}}{\partial t} + \mathbf{K} \mathbf{T} - \mathbf{F} = 0 \quad (11)$$

where  $\mathbf{T}$  is the vector of unknown nodal temperatures,  $\mathbf{C}$  the capacity matrix,  $\mathbf{L}$  the latent heat vector,  $\mathbf{K}$  the conductivity (stiffness) matrix and  $\mathbf{F}$  the external flux vector.

Each term of the residual vector  $\Psi$  is given (in components) by:

$$\begin{aligned} C_{ij} &= \int_{\Omega} \rho c N_i N_j dV \\ L_i &= \int_{\Omega} \rho \mathcal{L} f_l N_i dV \\ K_{ij} &= \int_{\Omega} \kappa \nabla N_i \cdot \nabla N_j dV + \int_{\partial\Omega_c} h_{env} N_i N_j dS. \end{aligned} \quad (12)$$

On the other hand, the load vector  $F$  takes the form:

$$F_i = - \int_{\partial\Omega_q} \bar{q} N_i dS + \int_{\partial\Omega_c} h_{env} T_{env} N_i dS - \int_{\partial\Omega} q N_i dV \quad (13)$$

The transient conduction problem in the absence of phase change has been widely discussed in the classic finite element literature (see e.g. [Zienkiewicz and Taylor \(2000\)](#)).

We follow the discontinuous integration scheme given in [Fachinotti et al. \(1999, 2001\)](#) that allows us to solve exactly the integrals (12) in a relatively easy manner.

### 3.3 Solution scheme

Time integration is done with the unconditionally stable first-order backward Euler method. This implicit scheme is applied on equation (11), which leads to a set of non-linear equations to be solved for the values of the temperatures at finite element nodes, at the end of the time increment considered:

$$\Psi_{n+1} = C_{n+1} \frac{T_{n+1} - T_n}{\Delta t} + \frac{L_{n+1} - L_n}{\Delta t} + K_{n+1} T_{n+1} - F_{n+1} = \mathbf{0} \quad (14)$$

The solution of the highly non-linear discrete balance equation (14) is achieved by means of the well-known Newton-Raphson method.

At each new iteration  $i$ ,  $\Psi$  is approximated using a first order Taylor expansion,

$$\Psi_{(T^{(i)})} \approx \Psi_{(T^{(i-1)})} + J_{(T^{(i-1)})} \Delta T^{(i)} = \mathbf{0} \quad (15)$$

being  $J = d\Psi/dT$  the Jacobian or tangent matrix of the equation system (14), and  $\Delta T^{(i)} = T^{(i)} - T^{(i-1)}$  the incremental correction of temperatures. Thus,  $\Delta T$  can be evaluated as follows:

$$\Delta T^{(i)} = -[J_{(T^{(i-1)})}]^{-1} \Psi_{(T^{(i-1)})} \quad (16)$$

The Newton-Raphson scheme is efficient provided that the initial guess  $T^{(0)}$  lies within the convergence radius of the solution  $T$ . Alternatively, the convergence can be improved using a line-search procedure.

Verification of the model has been performed comparing numerical and analytical results for a transient non-linear heat transfer problem with exact solution. This problem was solved exactly by [Özisik and Uzzell \(1979\)](#) and the numerical results, in agreement with the corresponding analytical ones are reported in [Anca et al. \(2004\)](#)

### 3.4 Heat Source Modeling in Welding

The moving heat source is implemented as a typical transient formulation where the heat source moves along the part with time. In order to model the heat source the three-dimensional double ellipsoid proposed by Goldak et al. (1984) as shown in Figure 3 is studied. One characteristic of the double ellipsoid geometry is that it can be easily changed to model both the shallow penetration arc welding processes and the deeper penetration laser and electron beam processes. The heat flux distribution is Gaussian along the longitudinal axis. The front half of the source is a quadrant of one ellipsoidal source while the rear half is a quadrant of another ellipsoidal source. Four parameters define each ellipsoid. Physically, they correspond to the dimensions of the molten zone. Knowing the cross-section of the molten zone from experiment, the heat source parameters can be determined. As a first approximation, Goldak et al. (1984) assume that it is reasonable to take the distance in front of the source equal to one half of the weld width and the distance behind the source equal to twice the weld width.

In order to simulate arc heating effects the equivalent heat input is assumed as a constant internal heat generation per unit volume.

It is convenient to introduce a coordinate,  $\xi$ , fixed on the heat source and moving with it. The moving reference frame on the heat source is related to the coordinate fixed on the work piece by:

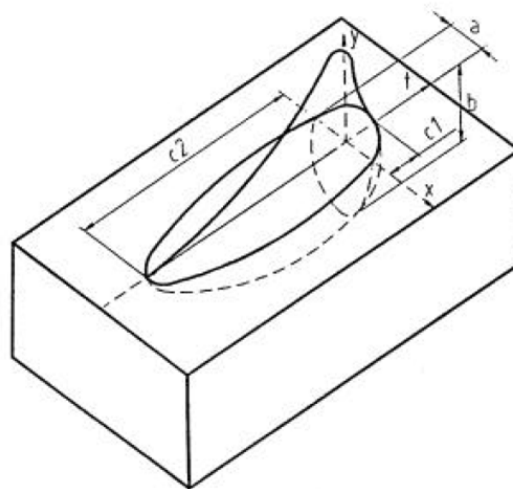


Figure 3: Goldak double ellipsoid heat source.

$$\xi = z - v(t - \tau) \quad (17)$$

where  $v$  is the welding speed and  $\tau$  is the time lag necessary to define the position of the heat source at time  $t = 0$ . The weighting fractions associated with the front and rear ellipsoids are denoted by  $f_f$  and  $f_r$ , respectively, and these fractions are specified to satisfy  $f_f + f_r = 2$ . Let us denote  $q$  the power density in  $W/m^3$  within the ellipsoid, and let  $a$ ,  $b$  and  $c$  denote the semi-axes of the ellipsoid parallel to the  $x$ ,  $y$ ,  $\xi$  axes. Then, the power density distribution inside the front quadrant, is specified by

$$q(x, y, \xi) = \left( \frac{6\sqrt{3}f_f Q}{abc_f \pi \sqrt{\pi}} \right) \exp\left(-3\frac{x^2}{a^2}\right) \exp\left(-3\frac{y^2}{b^2}\right) \exp\left(-3\frac{\xi^2}{c_f^2}\right) \quad (18)$$

and in the rear quadrant is specified by

$$q(x, y, \xi) = \left( \frac{6\sqrt{3}f_f Q}{abc_r \pi \sqrt{\pi}} \right) \exp\left(-3\frac{x^2}{a^2}\right) \exp\left(-3\frac{y^2}{b^2}\right) \exp\left(-3\frac{\xi^2}{c_r^2}\right) \quad (19)$$

In these equations,  $Q$  is the heat available at the source. For an electric arc the heat available is

$$Q = \eta VI \quad (20)$$

where  $\eta$  is the heat source efficiency,  $V$  is the arc voltage, and  $I$  is the arc current. The parameters  $a$ ,  $b$ ,  $c_f$  and  $c_r$  are independent, and can take different values for the front and rear quadrants of the source, to properly model the weld arc. One characteristic of this model is that start and stop effects of the heat source can be taken into account.

The spatial distribution of heat is calculated from equations (18) and (19) and is applied as a volumetric heat generation.

### 3.5 Verification

In order to verify the developed moving heat source model, a 3D finite element model of a thick plate was generated. Because of symmetry, one half of the welding plate was meshed. Figure 4 shows the problem geometry used in the 3D FEM analysis.

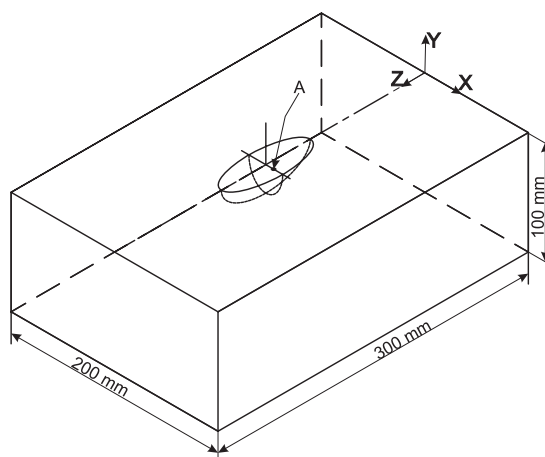


Figure 4: Geometry used in the 3D FEM verification analysis.

The model uses the same heat source distribution and material properties as those in Goldak's work and are summarized in tables 1, 2 and 3.

Arc Parameter	Symbol	Value	Unit
Current	$I$	1170	$A$
Voltage	$U$	32.9	$V$
Efficiency	$\eta$	0.95	—
Total Heat	$Q$	36538.35	$W$
Speed	$v$	5	$mm/s$

Table 1: Arc parameters.

Parameter	Value	Unit
a	20	mm
b	20	mm
cf	15	mm
cr	30	mm
ff	0.6	—
fr	1.4	—

Table 2: Goldak's Parameters.

Parameter	Symbol	Value	Unit
Density	$\rho$	7200.0	$[kg/m^3]$
Specific Heat, (solid)	$c_s$	680.0	$[J/kg^\circ K]$
Specific Heat, (liquid)	$c_l$	680.0	$[J/kg^\circ K]$
Latent Heat	$\mathcal{L}$	291660	$[J/kg]$
Conductivity (solid)	$\kappa_s$	34.0	$[W/m^\circ K]$
Conductivity (liquid)	$\kappa_l$	$2\kappa_s$	$[W/m^\circ C]$
Solidus temp.	$T_{sol}$	1774	$[^\circ K]$
Liquidus temp.	$T_{liq}$	1763	$[^\circ K]$
Initial temp.	$T_0$	283	$[^\circ K]$

Table 3: Material data for thermal problem.

Figure 5 plots the top surface temperature distribution along the  $x$  axis 11.5 seconds after the arc has passed. The numerical results we have computed are compared with the experimental test of Christensen et al. (1965).

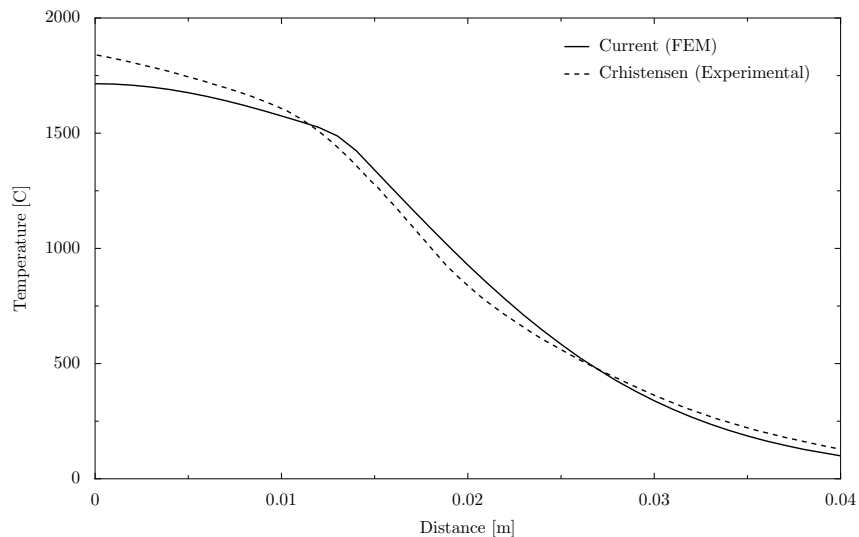


Figure 5: Comparison of the present model solution with Christensen experimental results.

#### 4 MECHANICAL PROBLEM

During a thermal welding process, the weld site and immediate surrounding area experience different rates of heating/cooling and thus expansion/contraction. This effect leads to consid-

erable thermal strains. Due to the heat application localized nature, the expansion due to these strains is constrained by the cool material away from the site of the applied heat. The physical and chemical properties of the material also change at the weld site and heat affected zone (HAZ), both during and after the welding process. These changes affect mechanical material properties, and must be taken into account in the mechanical analysis.

Due to the intrinsic three-dimensional nature of loads, boundary conditions and geometry usually involved in welding processes, a 3D mechanical model was implemented. It should be noted that the weld pool itself is not modelled in the mechanical analysis. This is only a soft region serving as a mean for heat input to the thermomechanical model. In this sense, the use of a cut-off or zero-strength temperature,  $ZST$ , was assumed. This is also the temperature above which no further changes in material properties are accounted for in the mechanical analysis.

The thermoelastic material behavior is, for most cases, based on a hypoelastic version of Hooke's law with inclusion of thermal strains. The Young's modulus and the thermal dilatation coefficient, are the most important parameters. Poisson ratio has a smaller influence on the residual stresses and deformations (Tekriwal and Mazumder., 1991). The plastic material model used for solidified metal was a rate-independent model with an associative J2 von Mises law and isotropic hardening. The argument for using rate-independent plasticity at high temperatures is based on the involved time scales (Lindgren, 2001). In the weld thermal cycle the material has a high temperature during a relatively short time, and therefore the accumulated rate-dependent plasticity may be neglected.

Inertial effects are ignored in momentum balance equations, according to the assumption of null acceleration within the solid.

#### 4.1 Melting-Solidifying Behavior

It is recognized that finite element techniques, with standard constitutive material modelling, yield good solutions in thermal stress analysis, even when the solid is subjected to temperatures near the solidification ones. However, there are particular aspects in the formulation for melting/solidifying problems that need to be carefully considered.

Three different configurations for every material point and its neighborhood (Figure 6) are considered for the mechanical simulation of this process:

- i) the reference configuration ( $B$ ), in which the particle label is assigned;
- ii) the (intermediate) natural configuration ( $B^0$ ) which corresponds to that state where the material point solidified just below the zero strength temperature ( $ZST$ ), and started to develop mechanical strength;
- iii) the current configuration ( $B^t$ ).

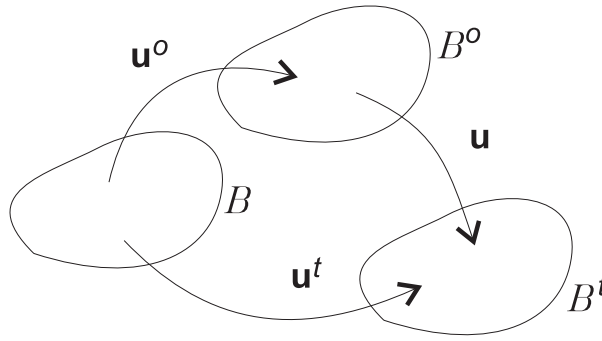


Figure 6: Reference ( $B$ ), natural ( $B^0$ ) and current ( $B^t$ ) body configurations in the melting/solidification problem.

Note that, since the solidification time instant is not the same one for all points in the domain of analysis, each material point has its own (intermediate) natural configuration.

Defining  $\mathbf{u}^o$  as the displacement from the reference to the natural configuration,  $\mathbf{u}^t$  the displacement from the reference to the current configuration and  $\mathbf{u}$  the displacement from the natural to the current configuration, one can write:

$$\mathbf{u}^t = \mathbf{u} + \mathbf{u}^o \tag{21}$$

Usually, when a finite element procedure is used, the mesh is defined in the reference configuration (the set of points at time  $t = 0$ ) as depicted schematically in Figure 6.

Let us consider that  $\mathbf{X}$  and  $\mathbf{x}^o$  are coordinate systems in the reference and natural configurations, respectively. As a consequence of the assumption of small deformations introduced to describe motion, and by assuming the existence of the intermediate deformation gradient in the neighborhood of every point, one has:  $\nabla_{\mathbf{X}} \mathbf{x}^o \approx \mathbb{I}$ . The same assumption allows us to evaluate the strain  $\boldsymbol{\varepsilon} = \nabla_{\mathbf{x}^o}^{sym} \mathbf{u}$ , related to the motion from the natural to the final configurations, by the following approximation:

$$\boldsymbol{\varepsilon} = \nabla_{\mathbf{x}^o}^{sym} \mathbf{u} \approx \nabla_{\mathbf{X}}^{sym} \mathbf{u} \tag{22}$$

By taking gradients in equation (21) and using the assumptions stated above, we can verify the validity of the additive decomposition of strains:

$$\boldsymbol{\varepsilon}^t = \boldsymbol{\varepsilon} + \boldsymbol{\varepsilon}^o \tag{23}$$

where  $\boldsymbol{\varepsilon}^t = \nabla_{\mathbf{X}}^{sym} \mathbf{u}^t$  is the strain tensor at the actual configuration (time  $t$ ) with respect to the reference configuration, and  $\boldsymbol{\varepsilon}^o = \nabla_{\mathbf{X}}^{sym} \mathbf{u}^o$  is the strain at the natural configuration with respect to the reference one.

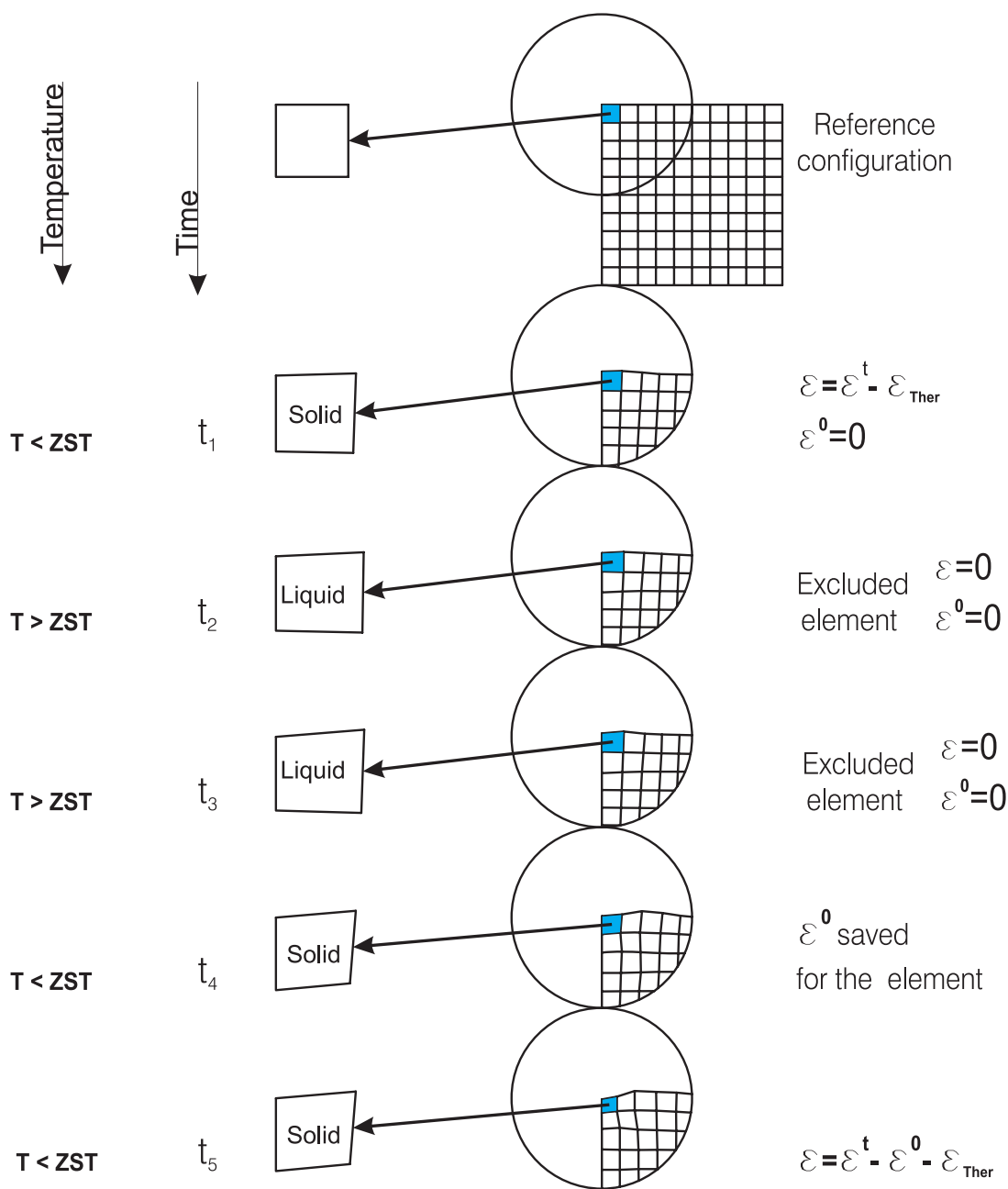


Figure 7: Evolution of d.o.f.s and strains in melting/solidification problems.

Stresses in the solid shell are directly related to the mechanical strains through the constitutive material law.

In order to test the formulation we selected a standard elastoplastic model, based on the classical  $J_2$  theory with isotropic hardening (Simo and Hughes, 1998) and the von Mises yield criteria.

We remark that for a correct representation of the steel constitutive behavior in the zone of interest, it is mandatory to account for the strong dependence of the material parameters on temperature.

**Remarks:**

- The strain  $\varepsilon^o$  is computed the first time that all nodal temperatures of the considered element fall below the zero strength temperature (ZST), and is stored at the finite element Gauss point as an additional tensorial internal variable. The *Zero Strength Temperature* is defined as the minimum temperature amongst those at which strength is zero (Nakagawa et al., 1995). In this work ZST is set equal to the metal solidus temperature.
- In this model, the solid phase domain changes with time. This fact introduces some difficulties concerning the mesh definition for the FE analysis. The procedure we have implemented consists in defining a fixed mesh that describes the complete domain, including the liquid and mushy zones. Nodes in the liquid and mushy zones are initially fixed. In subsequent time steps, when the nodal temperatures fall below the ZST, nodal d.o.f.'s are freed and the stiffness contribution of the solidified zone is taken into consideration (see Figure 7).
- The described numerical model does not predict the real displacement field inside the solid phase, because the displacement field of the natural configuration is not recorded.
- The technique of subtraction of the strain term  $\varepsilon^o$  from the total strain  $\varepsilon^t$  must be emphasized for its simplicity and accuracy. Stress computations based on total strain without subtraction of the initial strain  $\varepsilon^o$ , give completely unrealistic results, a fact that may be verified by comparison with results obtained by using the semi-analytical formulation of Weiner and Boley (1963). Note also that this approach is less expensive than those used by other authors based on recording the flow strain for liquid elements (Abid and Siddique, 2005; Yaghi and Becker, 2004).
- All elements internal variables, included the  $\varepsilon^o$  strain, are set to zero as soon as the element temperature rises above ZST.
- Mechanical elements have a special treatment during the liquid/solid and solid/liquid phase changes: while the temperature is above the ZST, the corresponding elemental d.o.f.'s are not included in the system of equations for the unknowns of the mechanical problem. This methodology incorporates an advantage compared to other techniques found in literature (e.g. assigning a very low stiffness to the elements that are in liquid/mushy phases, brings poor conditioning of the algebraic equation system to be solved).

To avoid restructuring the stiffness matrix each time step, liquid mechanical d.o.f.'s are decoupled from the rest by zeroing the corresponding rows and columns, and putting a non-zero term in the diagonal entry of the stiffness matrix. Also, the corresponding position in the residue is zeroed.

Figure 8(a) shows the initial stiffness matrix distribution when all domain is solid. Figures 8 (b), (c) and (d) show an increase in the decoupled rows as the solid domain decreases its size.

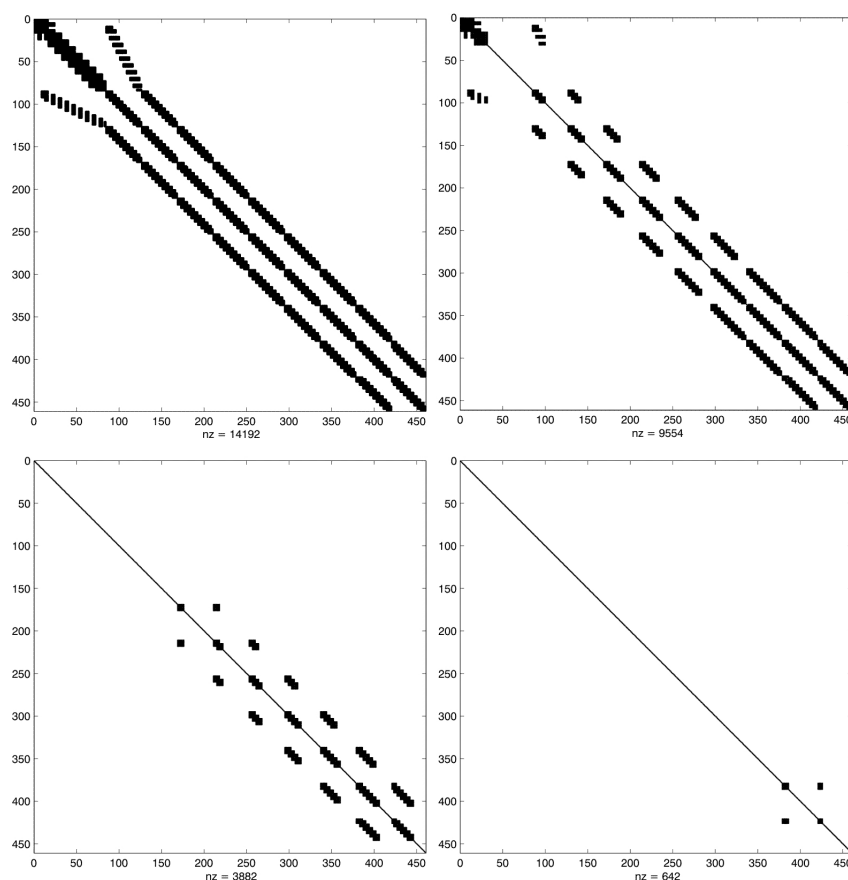


Figure 8: Matrix sparsity evolution.

## 4.2 Lagrangian formulation of the constitutive equations

According to the local state theory (Lemaître and Chaboche, 1994), at a given instant  $t$  the thermodynamic state at any particle  $\mathbf{X}$  of a material medium is completely defined by the values of a certain number of state variables at this particle. Computations on inelastic materials take advantage of strain-driven formulations, in which state variables are the strain  $\boldsymbol{\varepsilon}$  and a set of phenomenological internal strain-type variables describing material history, together with the temperature field  $T$  here assumed to be known a priori.

Linear kinematics is assumed. Then, the total strain can be additively decomposed as follows:

$$\boldsymbol{\varepsilon} = \boldsymbol{\varepsilon}^e + \boldsymbol{\varepsilon}^i, \quad (24)$$

$\boldsymbol{\varepsilon}^e$  being the thermoelastic (reversible) strain and  $\boldsymbol{\varepsilon}^i$  the inelastic (irreversible) strain. Either term may play the role of an internal variable, but  $\boldsymbol{\varepsilon}^i$  is typically chosen (option followed in this work).

We also adopt a scalar internal variable  $\alpha$ , which characterizes isotropic hardening from the phenomenological point of view. The hypothesis of isotropic hardening is widely accepted in welding applications (Lindgren, 2001; Francis and Rahman, 2000; Chang and Teng, 2004).

Furthermore, the adopted hardening parameter  $\alpha$  is the equivalent inelastic strain:

$$\alpha = \int_0^t \sqrt{\frac{2}{3}} \|\dot{\boldsymbol{\varepsilon}}^i(\tau)\| d\tau, \quad (25)$$

where  $\dot{\boldsymbol{\varepsilon}}^i$  is the inelastic strain rate and  $\|\dot{\boldsymbol{\varepsilon}}^i\| = \sqrt{\dot{\varepsilon}_{ij}^i \dot{\varepsilon}_{ij}^i}$  its  $L_2$ -norm.

Although driving variables lie in the strain space, response functions (i.e. the yield criterion and the evolution laws) are usually written in terms of their conjugated thermodynamic forces: the stress tensor  $\boldsymbol{\sigma}$  (dual of  $\boldsymbol{\varepsilon}^e$ ) and the isotropic hardening variable in stress space,  $R = R(\alpha)$ .

The stress tensor  $\boldsymbol{\sigma}$  depends on  $\boldsymbol{\varepsilon}$  and  $\boldsymbol{\varepsilon}^i$  through the decomposition (24). For linearly-elastic isotropic materials, the stress is defined by the state law:

$$\boldsymbol{\sigma} = \underbrace{\kappa [\text{tr}(\boldsymbol{\varepsilon}^e) - 3\varepsilon_{Ther}]}_{\sigma_m} \mathbb{I} + \underbrace{2\mu \text{dev}(\boldsymbol{\varepsilon}^e)}_{\boldsymbol{s}}, \quad (26)$$

where  $\kappa = \kappa(T)$  and  $\mu = \mu(T)$  are thermo-dependent material properties known as bulk and shear moduli, respectively,  $\varepsilon_{Ther}$  is the thermal strain,  $\mathbb{I}$  the second-order unit tensor,  $\text{tr}(\boldsymbol{\varepsilon}^e) = \varepsilon_{ii}^e$  and  $\text{dev}(\boldsymbol{\varepsilon}^e) = \boldsymbol{\varepsilon}^e - \text{tr}(\boldsymbol{\varepsilon}^e)\mathbb{I}/3$  are the trace and the deviator of the second-order tensor  $\boldsymbol{\varepsilon}^e$ ,  $\sigma_m = \text{tr}(\boldsymbol{\sigma})/3$  is the mean stress and  $\boldsymbol{s} = \text{dev}(\boldsymbol{\sigma})$  is the stress deviator. Here, the thermal expansion is defined by the thermal linear expansion (TLE) function:

$$\varepsilon_{Ther} = \text{TLE}(T) = \int_{T_{ref}}^T \alpha_T(\tau) d\tau, \quad (27)$$

with  $\alpha_T$  as the linear thermal expansion coefficient and  $T_{ref}$  an arbitrary reference temperature.

The von Mises criterion is defined:

$$f = \|\boldsymbol{s}\| - \sqrt{\frac{2}{3}} [\sigma_Y + R(\alpha)], \quad (28)$$

with  $\sigma_Y$  denoting the initial yield stress and  $R(\alpha)$  the hardening relation .

Associated to this yield criterion, the following  $J_2$  flow rule is considered:

$$\dot{\boldsymbol{\varepsilon}}^i = \gamma \boldsymbol{n}, \quad (29)$$

being  $\boldsymbol{n} = \boldsymbol{s}/\|\boldsymbol{s}\|$  the normalized stress deviator defining the normal to the Von Mises yield surface  $f = 0$  in the deviatoric-stress space, and  $\gamma \geq 0$  the consistency parameter. For plastic materials,  $\gamma$  is determined by means of the consistency condition

$$\gamma \dot{f} = 0. \quad (30)$$

Finally, having chosen the equivalent inelastic strain as hardening variable, the flow rule (29) completely defines the hardening law:

$$\dot{\alpha} = \sqrt{\frac{2}{3}} \|\dot{\boldsymbol{\varepsilon}}^i\| = \sqrt{\frac{2}{3}} \gamma. \quad (31)$$

### 4.3 Integration of the evolution equations

Following Simo and Hughes (1998), the evolution laws (29) and (31) are discretized using the implicit Euler-backward finite-difference scheme. Then, given the total strain increment  $\Delta\boldsymbol{\varepsilon}$  at the particle  $\boldsymbol{X}$  during the time interval  $[t_n, t_{n+1}]$ ,  $t_{n+1} = t_n + \Delta t$ , the material state at  $\boldsymbol{X}$  is updated from the previous instant  $t_n$  to the current one  $t_{n+1}$  by a standard return-mapping algorithm.

The consistent tangent stiffness matrix was implemented. The correct evaluation of this matrix is essential to achieve good numerical response in the determination of equilibrium condition.

#### 4.4 Finite element implementation

Ignoring inertial effects, momentum balance equation can be written as:

$$\nabla \cdot \boldsymbol{\sigma} + \rho \mathbf{b} = 0 \quad \forall \mathbf{X} \in \Omega_s, \quad (32)$$

subjected to the following boundary conditions

$$\mathbf{u} = \bar{\mathbf{u}} \quad \forall \mathbf{X} \in \partial\Omega_{s,u} \quad (33)$$

$$\boldsymbol{\sigma} \cdot \mathbf{n} = \bar{\mathbf{t}} \quad \forall \mathbf{X} \in \partial\Omega_{s,t}, \quad (34)$$

These lead to the standard quasi-static boundary value problem in solid mechanics (Hughes, 1987) which consists in finding the displacement field  $\mathbf{u}$  that satisfies the integral equations

$$\int_{\Omega_s} \boldsymbol{\sigma} : \nabla^s \mathbf{w} dV = \int_{\Omega_s} \rho \mathbf{b} \cdot \mathbf{w} dV + \int_{\partial\Omega_{s,t}} \bar{\mathbf{t}} \cdot \mathbf{w} dS, \quad (35)$$

throughout the domain  $\Omega_s$ , for all the admissible displacement weighting functions  $\mathbf{w}$ .

Equation (35) is the weak form of the momentum balance equations (32), where  $\rho \mathbf{b}$  is the body-force (per unit volume) and  $\bar{\mathbf{t}}$  is the traction prescribed over the portion  $\partial\Omega_{s,t}$  of the boundary (displacement boundary conditions over the complementary portion  $\partial\Omega_{s,u}$  are assumed to hold a priori).

The displacement trial functions are defined as follows:

$$\mathbf{u} = \sum_{i=1}^{n_u} N_i \mathbf{U}_i \quad (36)$$

being  $N_i$  the displacement shape function associated to the node  $i = 1, 2, \dots, n_u$ , being  $\mathbf{U}_i$  the nodal displacement

After replacing  $\mathbf{u}$  in (35) by its respective finite element approximation (36), and by adopting the shape functions as weight functions (Galerkin formulation), it yields

$$\mathbf{R} = \mathbf{F}_{int} - \mathbf{F}_{ext} = \mathbf{0}, \quad (37)$$

where

$$\mathbf{F}_{int} = \int_{\Omega_s} \mathbf{B}^T \boldsymbol{\sigma}(u) dV \quad (38)$$

$$\mathbf{F}_{ext} = \int_{\Omega_s} \mathbf{N}^T \rho \mathbf{b} dV + \int_{\partial\Omega_{s,t}} \mathbf{N}^T \bar{\mathbf{t}} dS \quad (39)$$

Being  $\mathbf{B}$  the typical finite element matrix defining the strain-displacement kinematics relation  $\boldsymbol{\varepsilon}^t = \mathbf{B}\mathbf{U}$ .

The nonlinear system of equations (37) is solved iteratively, approximating this system at the  $i$ -th iteration using a linear Taylor expansion

$$\mathbf{R}_{(\mathbf{U}^{(i)})} \approx \mathbf{R}_{(\mathbf{U}^{(i-1)})} + \mathbf{J}_{(\mathbf{U}^{(i-1)})} \Delta \mathbf{U}^{(i)} = \mathbf{0} \quad (40)$$

where  $\mathbf{J} = d\mathbf{R}/d\mathbf{U}$  is the Jacobian or tangent matrix, and  $\Delta \mathbf{U}^{(i)} = \mathbf{U}^{(i)} - \mathbf{U}^{(i-1)}$  is the search direction. Iterative correction of variables is defined by:

$$\Delta \mathbf{U}^{(i)} = -[\mathbf{J}_{(\mathbf{U}^{(i-1)})}]^{-1} \mathbf{R}_{(\mathbf{U}^{(i-1)})} \quad (41)$$

As described for the thermal problem, this Newton-Raphson scheme is complemented with line-search procedures to accelerate the convergence.

#### 4.4.1 Mixed $u$ - $p$ Formulation

Incompressible material behavior may lead to some difficulties in numerical simulation, such as volumetric locking, inaccuracy of solution, checkerboard pattern of stress distributions, or occasionally, divergence. Mixed  $u$ - $p$  elements are intended to overcome these problems. Mixed  $u$ - $p$  elements use both, displacements and hydrostatic pressure as primary unknown variables.

The standard quasi-static boundary value problem in solid mechanics, stated in mixed  $u$ - $p$  form (Hughes, 1987), consists in finding the displacement field  $\mathbf{u}$  and the mean-stress field  $p$  that satisfy the integral equations

$$\int_{\Omega} \boldsymbol{\sigma}_{dev} \text{grad } \mathbf{w} \, dV + \int_{\Omega} p \text{div } \mathbf{w} \, dV = \int_{\Omega} \rho \mathbf{b} \cdot \mathbf{w} \, dV + \int_{\partial\Omega_{\sigma}} \bar{\mathbf{t}} \cdot \mathbf{w} \, dS, \quad (42)$$

$$\int_{\Omega} \left[ \text{tr}(\boldsymbol{\varepsilon}_M) - \frac{p}{\kappa} \right] q \, dV = 0, \quad (43)$$

throughout the domain  $\Omega$ , for all the admissible displacement and mean-stress weighting functions  $\mathbf{w}$  and  $q$ , respectively.

Equation (42) is the weak form of the momentum balance equations, where  $\rho \mathbf{b}$  is the body-force (per unit volume) and  $\bar{\mathbf{t}}$  is the traction prescribed over the portion  $\partial\Omega_{\sigma}$  of the boundary (displacement boundary conditions over the complementary portion  $\partial\Omega_u$  are assumed to hold a priori).

The displacement and mean-stress trial functions are defined as follows:

$$\mathbf{u} = \sum_{i=1}^{n_u} N_i \mathbf{U}_i = \mathbf{N} \mathbf{U}, \quad (44)$$

$$p = \sum_{j=1}^{n_p} N_{p,j} P_j = \mathbf{N}_p \mathbf{P}, \quad (45)$$

$N_i$  being the displacement shape function associated to the displacement node  $i = 1, 2, \dots, n_u$ ,  $\mathbf{U}_i$  the nodal displacement,  $N_{p,j}$  the mean-stress shape function associated to the mean-stress node  $j = 1, 2, \dots, n_p$ , and  $P_j$  the nodal mean stress.

Appropriate mixed finite elements should be employed in order to deal with the numerical difficulties eventually caused by the inelastically-incompressible behavior of metals. We refer to the classical finite element literature (Hughes, 1987; Zienkiewicz and Taylor, 2000) for a detailed discussion of admissible  $u$ - and  $p$ -shape functions that guarantee the fulfillment of the Babuška-Brezzi stability conditions.

After replacing  $\mathbf{u}$  and  $p$  by their respective finite element approximations, and by adopting the corresponding shape functions as weight functions (Galerkin formulation), it yields

$$\mathbf{R}_1 = \mathbf{F}_{int} - \mathbf{F}_{ext} = \mathbf{0}, \quad (46)$$

$$\mathbf{R}_2 = \mathbf{K}_p^T \mathbf{U} - \mathbf{M}_p \mathbf{P} = \mathbf{0}, \quad (47)$$

where

$$\mathbf{F}_{int} = \int_{\Omega} \mathbf{B}^T \boldsymbol{\sigma}_{dev} dV + \mathbf{K}_p \mathbf{P}, \quad (48)$$

$$\mathbf{F}_{ext} = \int_{\Omega} \mathbf{N}^T \rho \mathbf{b} dV + \int_{\partial\Omega_{\sigma}} \mathbf{N}^T \bar{\mathbf{t}} dS, \quad (49)$$

$$\mathbf{K}_p = \int_{\Omega} \mathbf{B}^T \mathbb{I} \mathbf{N}_p dV, \quad (50)$$

$$\mathbf{M}_p = \int_{\Omega} \frac{1}{\kappa} \mathbf{N}_p^T \mathbf{N}_p dV, \quad (51)$$

$$(52)$$

In the above equations, symmetric second order tensors like the stress deviator  $\boldsymbol{\sigma}_{dev}$  and the unit tensor  $\mathbb{I}$  are mapped into vectors as usually done in the finite element practice, and  $\mathbf{B}$  is the typical finite element matrix defining the shape functions derivative.

If the material is only nearly incompressible and the pressure variables are considered on the elemental level only then the pressure terms can be statically condensed out and solved for displacements only.

As pointed out by [Cifuentes and Kalbag \(1992\)](#); [Benzley et al. \(1995\)](#), hexahedral elements are superior to linear tetrahedral elements, and also better than quadratic tetrahedron elements when plastic deformation occurs, and therefore we used  $q1 - p0$  hexahedral elements to do the tests.

The discrete equilibrium equations are solved by using a standard Newton-Raphson method. The Jacobian matrix corresponds to that obtained from an equivalent purely Lagrangian elasto-plastic quasi-static incremental problem (see for instance [Simo et al. \(1998\)](#)).

#### 4.5 Validation of the model

The thermal stress calculated by the finite element model developed in the present work has been compared with the semi-analytical solution developed by [Weiner and Boley \(1963\)](#) for thermal stresses during one-dimensional solidification of a semi-infinite elastic-perfectly plastic body after a sudden decrease in surface temperature.

The thermal problem they solved corresponds to the Neumann's classical one, a phase change 1D problem with uniform initial temperature  $T_s$  (solidification temperature) and fixed temperature  $T_w < T_s$  on one end, being  $T^o = T_s - T_w$  defined as the temperature drop.

They took an elastic-perfectly plastic material model for the mechanical problem, with a constant Young modulus  $E$  and yield stress  $\sigma_y$  varying linearly with temperature:

$$\sigma_{y(T)} = \sigma_y^o \frac{T_s - T}{T^o} \quad ; \quad T \leq T_s \quad (53)$$

where  $\sigma_y^o$  is the yield stress at temperature  $T^o$ .

The Neumann's solution introduces a characteristic length  $\bar{y} = p\sqrt{t}$ , where  $t$  denotes time and the parameter  $p$  is given by:

$$p = 2\sqrt{K_s} \gamma \quad ; \quad K_s = \frac{\kappa}{\rho C_p} \quad ; \quad \gamma \approx \sqrt{\frac{T^o C_p}{2L}} \quad (\gamma^2 \ll 1); \quad (54)$$

The thermal diffusivity ( $K_s$ ) is the ratio of conductivity ( $\kappa$ ) to density ( $\rho$ ) and specific heat ( $C_p$ ), while  $L$  is the latent heat.

Weiner et al. introduced also the dimensionless quantities:

$$\hat{y} = \frac{y}{\bar{y}} \quad ; \quad \hat{T} = \frac{T - T_s}{T_o}$$

$$\hat{\sigma} = \frac{(1 - \nu)\sigma}{\alpha_T E T_o} \quad ; \quad \hat{\sigma}_y = \frac{(1 - \nu)\sigma_y}{\alpha_T E T_o} = -m\hat{T} \quad ; \quad m = \frac{(1 - \nu)\sigma_y^o}{\alpha_T E T_o}$$

where  $\alpha_T$  is the thermal expansion coefficient and  $\nu$  the Poisson ratio.

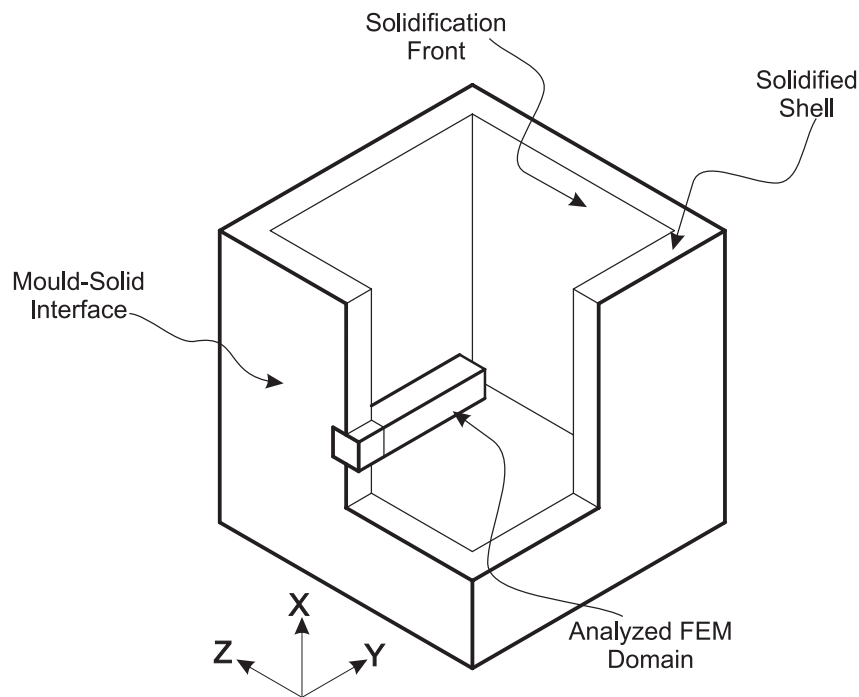


Figure 9: Weiner and Boley (1963) problem description.

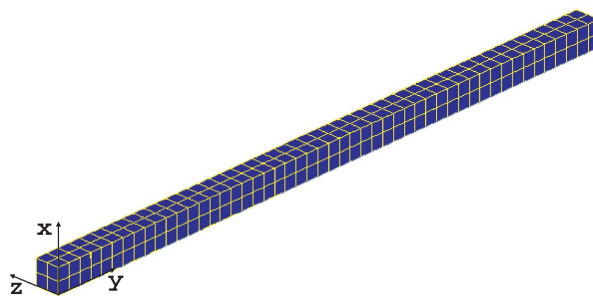


Figure 10: Finite element model for the 1-D numerical validation test.

The problem has been solved in a prismatic domain using the finite element procedure described in subsection 4.4, and imposing Extended Plane Strain (EPS) conditions ( $\varepsilon_x = \text{constant}$ ,  $\varepsilon_z = \text{constant}$ ) along transversal directions  $z$  and  $x$ , to be consistent with the original hypothesis proposed by Weiner et al.

The FE mesh consists in hexahedral elements, as shown in Figure 10. The EPS conditions are imposed via Lagrange multipliers, constraining all nodal  $x$ - and  $z$ -displacements to be identical.

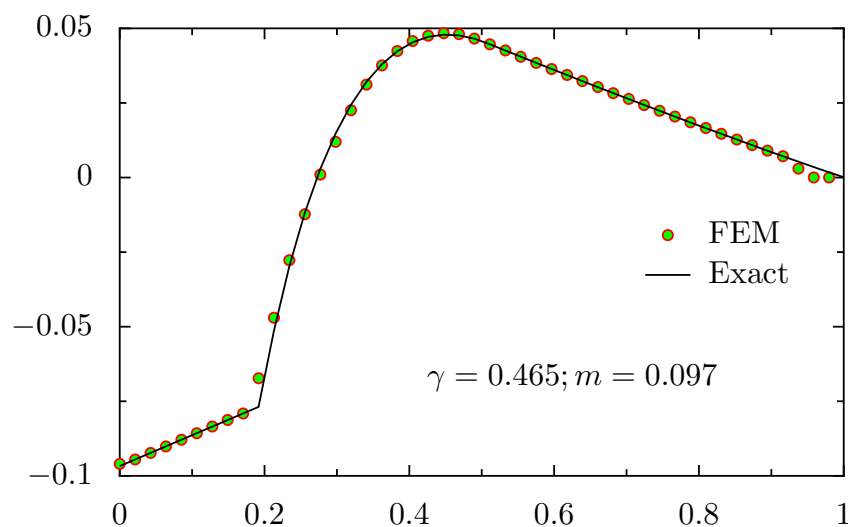


Figure 11: Stress distribution along the  $\hat{y}$ -coordinate. Comparison of semi-analytical (Weiner and Boley, 1963) and numerical solutions.

Figure 11 compares the semi-analytical results with the numerical ones. The curves plot the non-dimensional stress component  $\hat{\sigma}_{xx}$  ( $= \hat{\sigma}_{zz}$ ) along the non-dimensional  $\hat{y}$ -line (longitudinal direction) for  $m = 0.097$  and  $\gamma = 0.465$ . The agreement of the numerical FE solution with the semi-analytical one is evident from the figure.

It should be noted that this semi-analytical solution gives a maximum tensile (compressive) stress which is constant in time. This behavior is due to the particular thermal boundary conditions adopted (which correspond to a similarity solution) in the mentioned semi-analytical study.

## 5 SOLUTION SCHEME

Due to the weak nature of mechanical to thermal field coupling, the non-linear transient analysis is divided in two parts.

First, thermal analysis is performed to predict the temperature history of the whole domain, and then it is applied as input for the subsequent structural analysis.

The coupling is organized using a staggered scheme, where for every time step the thermal problem are solved first, and then the mechanical problem is solved using as inputs the temperature obtained previously, as shown in Figure 12.

Algorithm 1 shows the global calculation scheme. At the time being, a fixed time step is specified.

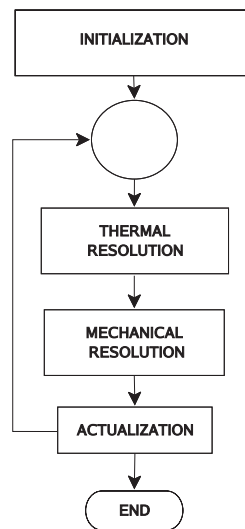


Figure 12: Thermo-mechanical solution scheme

**Algorithm 1** Staggered Solver

---

```

while  $t < t_{end}$  do
   $t = t + \Delta t$ 
  THERMAL_NEWTON
  while  $\|\Psi_{(T^{(i)})}\| > Tol_{ther}$  do
    Calculate  $\Delta T^{(i)} = -[J_{(T^{(i-1)})}]^{-1} \Psi_{(T^{(i-1)})}$ 
    Compute  $\Psi_{(T^{(i)})}$ 
  end while
  MECHANICAL_NEWTON
  while  $\|R_{(U^{(i)})}\| > Tol_{mech}$  do
    Calculate  $\Delta U^{(i)} = -[J_{(U^{(i-1)})}]^{-1} R_{(U^{(i-1)})}$ 
    Compute  $R_{(U^{(i)})}$ 
  end while
end while

```

---

**5.1 Mesh subdivision method**

As pointed out in Section 4 hexahedral finite elements are used to solve the mechanical problem. In the other hand, the thermal problem is solved using tetrahedral elements.

In order to share the same nodes in both problems, first a mesh of hexahedra for the mechanical model is generated. Then by splitting each hexahedron in six tetrahedra, as depicted in Figure 13, the thermal finite element mesh is obtained.

**6 APPLICATION EXAMPLES****6.1 Residual Stresses in Fusion Welding**

Residual stresses associated with thermal welding processes are of particular importance because they are frequently the same order of magnitude than yield stresses. Fatigue failure of welded structures occurs usually at the weld site, along or adjacent to the weld toe. Residual stresses and strains may also approach yield magnitude in the transverse direction to the weld.

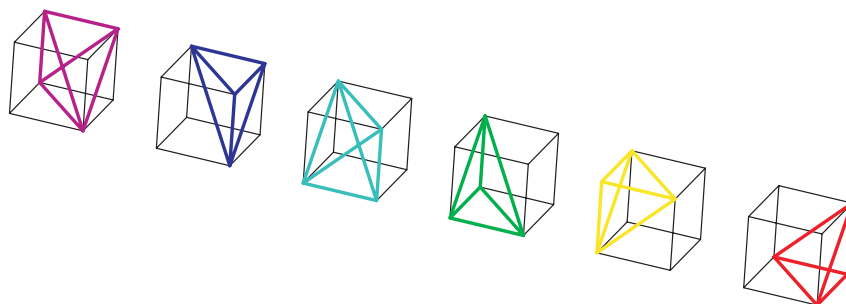


Figure 13: Subdivision of an hexahedron into six tetrahedra

The magnitude of the residual stresses and their distribution depends on numerous factors, including the type of welding, number of passes, material properties and degree of constraint during the process. Material that is rigidly constrained will have greater residual stresses than one that is allowed to distort during the process.

During a thermal welding process, the weld site and immediate surrounding area experience different rates of heating/cooling and thus expansion/contraction, and this leads to large thermal strains. Due to the heat application localized nature, the expansion due to these strains is constrained by the cooler material away from the site of the applied heat.

A stress parallel to the direction of the weld bead is called longitudinal residual stress, denoted by the letter  $\sigma_z$ . The longitudinal residual stress arises due to longitudinal expansion and contraction during welding. Along the weld line, a high tensile residual stress arises near the weld toe, and then decreases to zero, finally becoming compressive, as distance from the weld line on the flange increases.

A stress normal to the direction of the weld bead is known as a transverse residual stress, denoted by the letter  $\sigma_x$ . A tensile residual stress is produced at the surface of the specimen near the weld and decreasing close to zero as the distance from the weld toe increases.

## 6.2 Butt-welded Plates

In this example a butt-welded plate is presented with length, width and thickness respectively equal to  $L = 500\text{mm}$ ,  $W = 500\text{mm}$ ,  $th = 6\text{mm}$ . A 3-dimensional symmetrical model was used to estimate the residual stresses of the butt-welded joint using the finite element method.

The material properties used in the model correspond to a CMn steel. The plate is clamped in the corners opposite at the site to the welded line. Natural convection in top and bottom surfaces of the plate is assumed, with a heat transfer coefficient of  $45 \left[ \frac{W}{m^2K} \right]$ .

The welding parameters are summarized in table 4 and 5.

Arc Parameter	Symbol	Value	Unit
Current	$I$	250	$A$
Voltage	$U$	23	$V$
Efficiency	$\eta$	0.825	—
Total Heat	$Q$	4743.75	$W$
Speed	$v$	4.8	$mm/s$

Table 4: Arc parameters.

The symmetric model has 3750 elements and 6000 nodes after meshing.

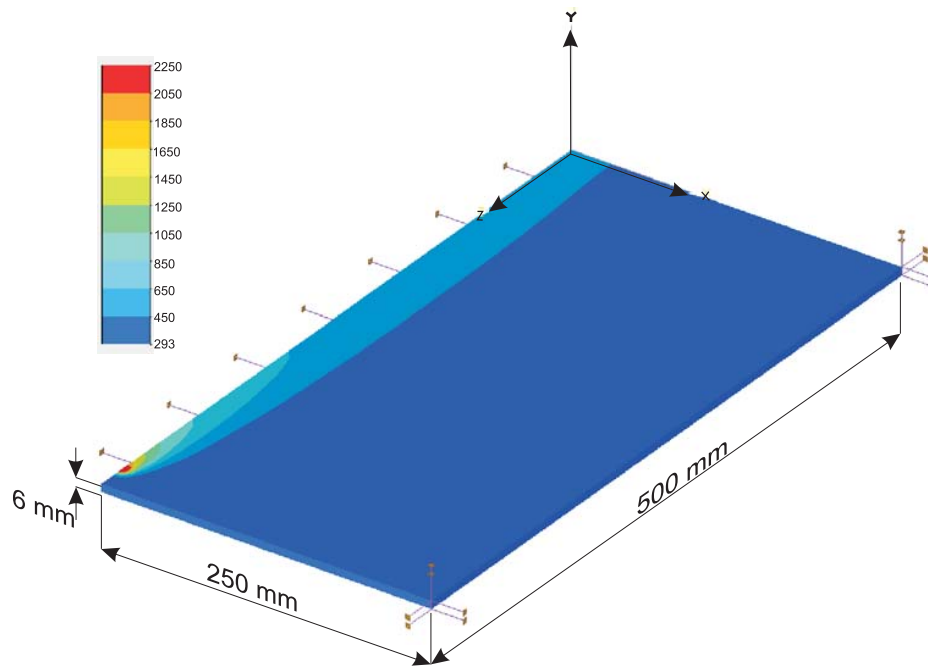
Goldak Parameter	Value	Unit
a	5	mm
b	3	mm
cf	5	mm
cr	10	mm
ff	0.6	—
fr	1.4	—

Table 5: Goldak's Parameters.

### 6.2.1 Simulation results

The process takes about 100 s to complete the weld. After extinguishing the arc, cooling of the weldment takes about 35 min to return to the ambient temperature. The time stepping has a minimum time step of 0.5 s during welding. The complete analysis has taken about 14 hs of CPU, on a Intel Core2 1.86 GHz processor.

The temperature results (Figure 14) shows that because of the locally concentrated heat source, the temperature near the weld bead and heat-affected zone rapidly changes with the distance from the centre of the heat source.

Figure 14: Temperature field [K] at time  $t = 100s$ .

Related to the residual stresses, Figures 15 and 16 show calculated longitudinal ( $\sigma_z$ ) and transverse ( $\sigma_x$ ) stresses. The behaviour is analogous to that found in the literature. As expected the maximum residual stress is produced near the heat affected zone. The longitudinal normal component of stress is in the order of the yield stress.

## 7 CONCLUSIONS

In the present article finite element models have been used to analyze the thermal and mechanical phenomena observed in welding processes. Thermal histories and residual stresses

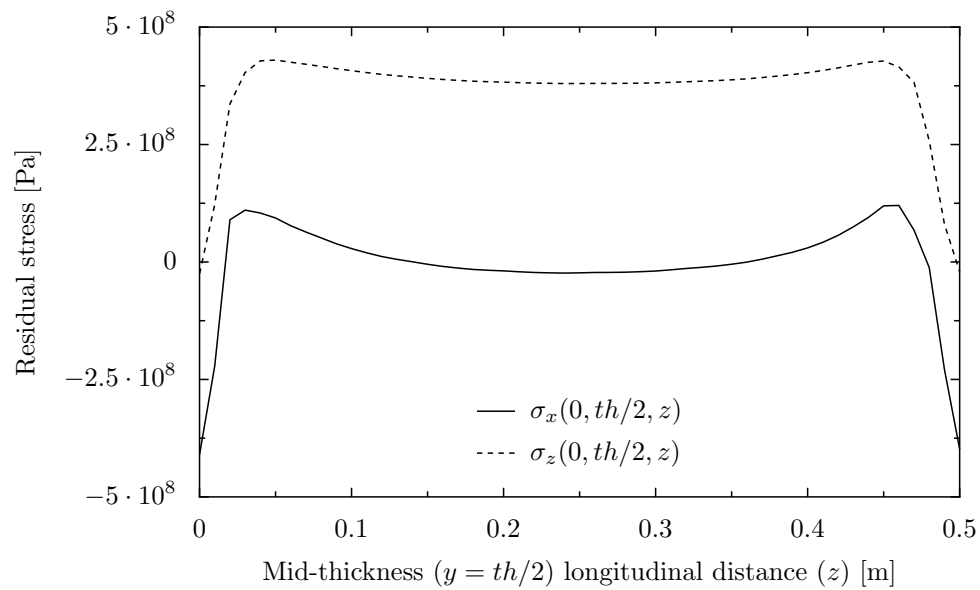


Figure 15: Residual stress distribution at  $t = 300s$  in a longitudinal section.

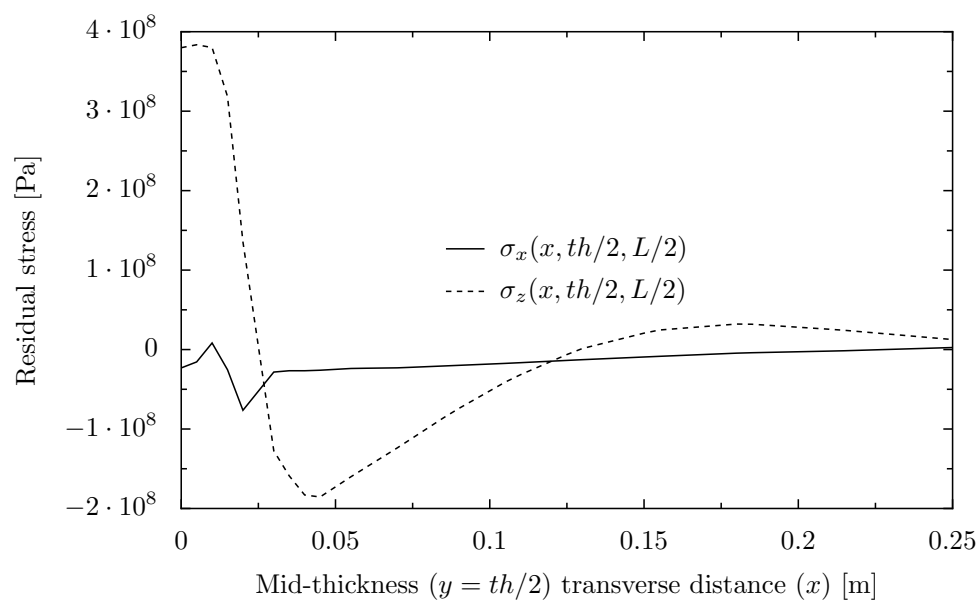


Figure 16: Residual stress distribution at  $t = 300s$  in an transversal section.

have been predicted.

The described methods provide a powerful means to optimize process parameters off-line. The welding model can be used to predict and minimize deformations due to changes in the weld sequence during the product development stage.

A mathematical model was implemented to represent the power density distribution of the external heat source. Results obtained in this work using the heat source model are in close agreement with the original results obtained by both, the experimental data of Christensen et al. (1965) and the ellipsoidal model proposed by Goldak et al. (1984).

A standard finite element formulation limited to the solid domain has been adopted for the mechanical analysis, proving to be effective. Regarding the material description, a standard model with isotropic hardening has proven to characterize well the behavior of steel at high temperatures.

In relation to the methodology described in Section 4.1 the melting/solidifying treatment of mechanical elements has proved to be satisfactory in validating the thermo-mechanical analysis of phase-change problems with the semi-analytical solution of Weiner and Boley (1963) as described in Section 4.5. This is a solid basement to continue software development with ability to simulate accurately complex welding processes.

The finite element models described were applied to solve the final residual stress state of a butt-welded joint.

## REFERENCES

- Abid M. and Siddique M. Numerical simulation to study the effect of tack welds and root gap on welding deformations and residual stresses of a pipe-flange joint. *International Journal of Pressure Vessels and Piping*, 82:860–871, 2005.
- Anca A., Cardona A., and Risso J. 3d thermo-mechanical simulation of welding processes. In G. Buscaglia, E. Dari, and O. Zamonsky, editors, *Mecánica Computacional, XIV Congreso de Métodos Numéricos y sus Aplicaciones (Enief 2004)*, volume XXIII, pages 2301–2318. 2004.
- Benzley S., Perry E., Merkely K., Clark B., and Sjaardama G. A comparison of all hexagonal and all tetrahedral finite element meshes for elastic and elasto-plastic analysis. *Proc. 14th Ann. Int. Meshing Roundtable, Albuquerque, USA*, 1995.
- Chang P. and Teng T. Numerical and experimental investigations on the residual stresses of the butt-welded joints. *Computational Materials Science*, 29(4):511–522, 2004.
- Christensen N., Davies V.d.L., and Gjermundsen K. Distribution of temperatures in arc welding. *British Welding Journal*, 12:54–75, 1965.
- Cifuentes A. and Kalbag A. A performance study of tetrahedral and hexahedral elements in 3-d finite element structural analysis. *Fin. Elem. Anal*, 12:313–318, 1992.
- Fachinotti V., Cardona A., and Huespe A. A fast convergent and accurate temperature model for phase-change heat conduction. *Int. J. Numer. Meth. Engng.*, 44:1863–1884, 1999.
- Fachinotti V., Cardona A., and Huespe A. Numerical simulation of conduction-advection problems with phase change. *Latin Am. Applied Research*, 31:31–36, 2001.
- Francis M. and Rahman S. Probabilistic analysis of weld cracks in center-cracked tension specimens. *Computers and Structures*, 76:483–506, 2000.
- Goldak J., Chakravarti A., and Bibby M. A new finite element model for welding heat sources. *Metallurgical Transactions B*, 15:299–305, 1984.
- Hughes T. *The Finite Element Method. Linear Static and Dynamic Finite Element Analysis*. Prentice-Hall, 1987.

- Lemaître J. and Chaboche J. *Mechanics of Solid Materials*. Cambridge University Press, 1994.
- Lindgren L.E. Finite element modeling and simulation of welding. part 2: Improved material modeling. *J. Thermal Stresses*, 24(3):195–231, 2001.
- Mackerle J. Finite element analysis and simulation of welding-an addendum: a bibliography (1996-2001). *Modelling Simul. Mater. Sci. Eng.*, 10:295–318, 2004.
- Nakagawa T., Umeda T., Murata J., Kamimura Y., and Niwa N. Deformation behavior during solidification of steels. *ISIJ Int.*, 35(6):723–729, 1995.
- Özisik M. and Uzzell J. Exact solution for freezing in cylindrical symmetry with extended freezing temperature range. *Journal of Heat Transfer*, 101:331–334, 1979.
- Simo J. and Hughes T. *Computational Inelasticity*. Springer-Verlag, New York, 1998.
- Tekriwal P. and Mazumder. J. Transient and residual thermal strain-stress analysis of gmaw. *ASME J. of Engineering Materials and Technology*, 113(336-343), 1991.
- Weiner J. and Boley B. Elasto-plastic thermal stresses in a solidifying body. *J. Mech. Phys. Solids*, 11:145–154, 1963.
- Yaghi A. and Becker A. State of the art review - weld simulation using finite element methods. Technical report, University of Nottingham, UK, 2004.
- Zienkiewicz O. and Taylor R. *The Finite Element Method*, volume 1: The Basis. Butterworth-Heinemann, 5th. edition, 2000.